

## RESEARCH ARTICLE

10.1029/2018JB017039

## Key Points:

- We detect and relocate 350 earthquakes associated with pre-hydraulic, cohydraulic, and post-hydraulic fracturing injection in northeast BC
- Induced earthquakes occurred within 4 km of the hydraulic fracturing wellbore, and migration pattern indicates a diffusivity of  $\sim 0.2 \text{ m}^2/\text{s}$
- Pore pressure diffusion controls seismicity at  $< 1 \text{ km}$ , and poroelastic stress transfer dominates at  $\sim 1\text{--}4 \text{ km}$

## Supporting Information:

- Supporting Information S1
- Figure S1
- Table S1
- Table S2
- Table S3

## Correspondence to:

H. Yu,  
hongyu.yu@rub.de

## Citation:

Yu, H., Harrington, R. M., Liu, Y., & Wang, B. (2019). Induced seismicity driven by fluid diffusion revealed by a near-field hydraulic stimulation monitoring array in the Montney Basin, British Columbia. *Journal of Geophysical Research: Solid Earth*, 124, 4694–4709. <https://doi.org/10.1029/2018JB017039>

Received 14 NOV 2018

Accepted 4 APR 2019

Accepted article online 9 APR 2019

Published online 3 MAY 2019

## Induced Seismicity Driven by Fluid Diffusion Revealed by a Near-Field Hydraulic Stimulation Monitoring Array in the Montney Basin, British Columbia

H. Yu<sup>1</sup> , R. M. Harrington<sup>1</sup> , Y. Liu<sup>2</sup> , and B. Wang<sup>1,2</sup>

<sup>1</sup>Institute for Geology, Mineralogy and Geophysics, Ruhr University Bochum, Bochum, Germany, <sup>2</sup>Earth and Planetary Sciences Department, McGill University, Montreal, Quebec, Canada

**Abstract** This study presents observations using new data from a deployment of eight broadband seismometers surrounding a horizontal well pad at distances of  $\sim 1\text{--}3 \text{ km}$  for the period before, during, and after a hydraulic fracturing treatment in the Montney Basin, British Columbia, Canada. We use a multistation-matched filter detection and double-difference earthquake relocation to develop a catalog of 350 events associated with hydraulic fracturing stimulation, with magnitudes ranging from  $-2.8$  to  $1.8$  and estimated catalog completeness of approximately  $-0.2$ . The seismicity distribution suggests a statistically significant association with injection, and event migration can be described by a hydraulic diffusivity of  $\sim 0.2 \text{ m}^2/\text{s}$ . A comparison between daily seismicity rate and analytical stress evolution inferred from daily injection volumes implies that pore pressure diffusion largely controls earthquake nucleation at distances less than  $1 \text{ km}$ , whereas poroelastic stress transfer likely dominates at intermediate distances of  $\sim 1\text{--}4 \text{ km}$  at time scales shorter than diffusion. Both mechanisms likely have a limited effect on stress perturbation at distances over  $5 \text{ km}$ .

### 1. Introduction

In the last decade, increased injection activity related to hydraulic fracturing (HF) and wastewater disposal (WD) has been linked to increased seismicity rates in North America (Atkinson et al., 2016; Ellsworth, 2013; Keranen et al., 2014; Rivard et al., 2014). WD generally produces larger magnitude events relative to HF, which is often attributed to the differences in injected volumes (Goebel, Weingarten, et al., 2017; Weingarten et al., 2015). While HF-induced earthquakes are typically minor ( $M < 4$ ; Clarke et al., 2014; Ellsworth, 2013; Holland, 2013; Skoumal et al., 2015), some recent events have exceeded  $M4$ , for example, the 2015  $M4.6$  earthquake in the Western Canadian Sedimentary Basin (WCSB; Mahani et al., 2017), the 2017  $M4.7$  Sichuan Basin earthquake (Lei et al., 2017), and the 2018  $M4.5$  earthquake in the WCSB, near Dawson Creek, BC (Roth et al., 2018), and the 2019  $M4.6$  earthquake in the Red Deer, AB (International Seismological Centre, 2019).

A number of physical mechanisms, including pore pressure diffusion, elastic shear and normal stress perturbations transferred via the rock matrix (often termed as poroelastic stresses), variations in lithology, or some combination of the above, have been proposed to influence stress perturbations resolved onto proximal faults. Pore pressure increase due to fluid diffusion has been considered a leading mechanism for explaining the spatial and temporal distribution of seismicity and is often used as the primary means of stress perturbation in hydrogeological models (e.g., BC Oil and Gas Commission, 2012; Healy et al., 1968; Keranen et al., 2014; Rayleigh et al., 1976; Shapiro & Dinske, 2009). In the context of pore pressure diffusion, effective normal stress (difference between normal stress and pore pressure) on preexisting faults can be decreased by raising pore fluid pressure, thereby lowering the failure threshold on critically stressed faults and promoting earthquakes (e.g., BC Oil and Gas Commission, 2012; Goebel et al., 2016; Healy et al., 1968; Horton, 2012; Rayleigh et al., 1976; Shapiro & Dinske, 2009; Zoback & Harjes, 1997). The temporal delay between the onset of pumping and fault slip nucleation can range from an immediate response to a delay of several years, suggesting a wide range of initial pore pressure conditions and effective hydraulic conductivities in rock formations (e.g., Altmann et al., 2013; Hsieh & Bredehoeft, 1981; Keranen et al., 2013; Martínez-Garzón et al., 2014). On the other hand, the poroelastic framework considers the fully coupled stress evolution of a saturated medium and thus considers elastic stress transfer via the rock matrix in addition to pore pressure diffusion. The poroelastic framework is thus better equipped to explain immediate stress perturbations at large

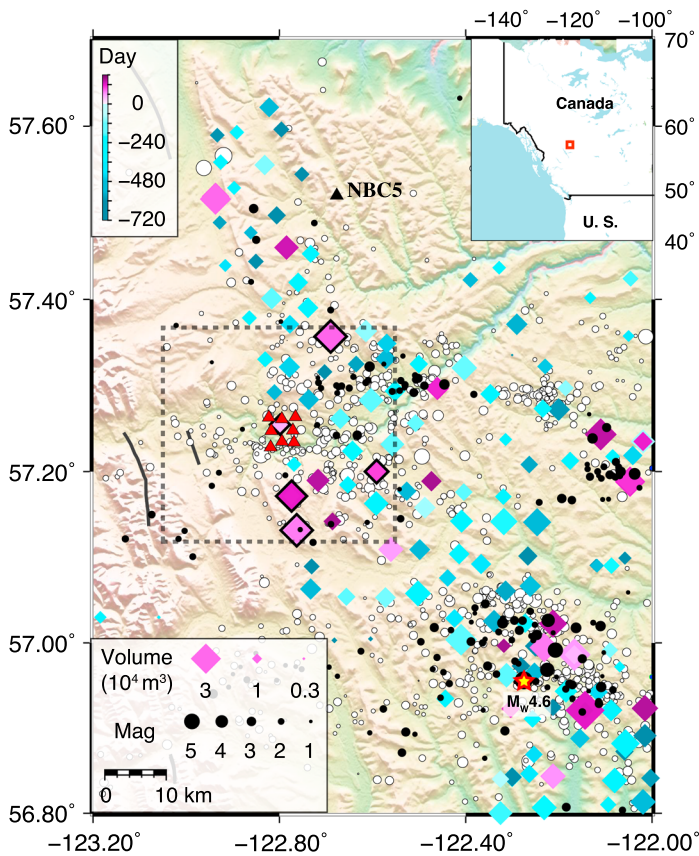


**Figure 1.** Hydraulic fracturing activity, seismicity, and station distribution in Montney Basin, northeast British Columbia, Canada. Red/black triangles show McGill/NRCAN seismic stations, respectively. Diamonds: active hydraulic fracturing wells reported by British Columbia Oil and Gas Commission, between 1 May 2013 and 1 November 2015. Size corresponds to the injection volume. Color bar indicates the hydraulic fracturing well operation date, with respect to the start of MG station deployment (28 May 2015). Diamonds with thick black edges indicate wells active during the station deployment period (28 May 2015 to 15 October 2015). Black/white dots: 1,108 earthquakes during/outside MG deployment period, between 1 January 2014 and 31 December 2016 cataloged by Visser et al. (2017). Star represents the 17 August 2015  $M_W$  4.6 hydraulic fracturing-induced earthquake near Fort St John. Dashed line box outlines 30 km \* 30 km area of this study. Inset shows the location of the Montney Basin within the Western Canadian Sedimentary Basin.

distances compared to fluid diffusion (Goebel, Weingarten, et al., 2017; Goebel & Brodsky, 2018; Kozłowska et al., 2018; Segall et al., 1994). In particular, such immediate stress increases are needed to explain observed events at distances of ~10 km or more that occur at time scales shorter than fluid diffusion times (e.g., Deng et al., 2016; Goebel, Weingarten, et al., 2017).

Studies also suggest that lithology may influence the physical mechanisms responsible for induced events and their spatial distribution. For example, Goebel and Brodsky (2018) suggested, based on a global compilation of well-recorded injection-induced earthquakes, that injection above the basement is associated with stronger fluid/matrix coupling in the soft sedimentary sequences and thus may provide more favorable conditions for poroelastic stress transfer. In contrast, fluid coupling may be weaker in the stiffer basement rocks, favoring pore pressure diffusion as a leading stress transfer mechanism. In Alberta, Schultz et al. (2016) found that hypocenters of HF-induced seismicity coincide with the margins of the Devonian carbonate reefs, suggesting nucleation preference to paleobathymetric highs associated with Precambrian basement tectonics.

The relative importance of fluid diffusion and poroelasticity-induced stress changes can be illustrated in the studies of short-period, high-rate injection into low permeability (tight) shale formations during hydraulic stimulation and its spatiotemporal correlation to induced earthquakes (Galloway et al., 2018; Kozłowska et al., 2018; Schultz et al., 2016; Shapiro & Dinske, 2009). However, many HF studies in the Central and Eastern United States are in locations where ongoing WD may also provide a strong imprint on the seismic response. In contrast, the lower volumes of coproduced wastewater in the WCSB result in a lower density of WD wells and provide a unique opportunity to isolate the effects of HF injection (Atkinson et al., 2016). The Montney shale formation is thus an appropriate area to conduct such studies. Located in northeastern British Columbia and northwestern Alberta, it is one of the main shale formations targeted for HF in Canada. This region has experienced a drastic increase in seismicity since 2005, as drilling activity increased rapidly (Rivard et al., 2014). For example, the number of M3+ events increased threefold from 2008 to 2015, including the 2015 M4.6, the 2018 M4.5, and the 2019 M4.6 earthquakes referenced above. While the seismic response to pumping has been vigorous in some places, the sparse permanent regional network is only capable of detecting earthquakes with magnitudes larger than  $\sim M_L 2.5$  (Visser et al., 2017), making it difficult to perform detailed analyses of hazard near individual wells (or groups of wells).

Here we present a detailed source parameter study of induced earthquakes associated with a HF stimulation in the Montney Basin area with no proximal disposal wells. We use new data from the deployment of eight broadband seismometers at distances ranging from ~1 to 3 km from the well pad of a horizontal well bore for a period bracketing 6 weeks prior to and 3 months following a HF stimulation in the Montney Basin area (Figure 1). The temporal coverage and the close event-station distances allow us to compile a multistation matched-filter (MMF) enhanced catalog and calculate double-difference earthquake relative relocations, in order to quantify the spatiotemporal distribution of earthquakes in response to fluid injection. We use relocated seismicity to highlight the geometry of seismically active structures and further investigate earthquake migration patterns and their source parameters to probe the nucleation mechanism(s). We also compare the histogram of detected seismicity with daily-averaged injection volumes in multiple nearby wells in order to identify temporal correlations. We observe two dominant event types: (1) high-frequency

(broadband) events analogous to “standard” tectonic earthquakes and (2) hybrid-type events that commence with an impulsive broadband signal and transition to low-frequency ringing. Here we focus on the results of the more numerous high-frequency events, whereas a follow-up study will focus solely on the source characteristics and physical mechanisms of the hybrid-type events.

## 2. Catalog Construction and Spatiotemporal Correlation to Fluid Injection

The data used for catalog building were recorded on eight Nanometrics Trillium Compact 20s broadband seismograph stations (MG01-08) deployed between 28 May 2015 to 15 October 2015 within 1–3 km from the well pad, in the northern Montney shale formation, British Columbia. Additional data come from one regional Canadian National Seismograph Network (CNSN) station, NBC5 (Figure 1). Continuous waveforms recorded ground velocity at a sampling rate of 100 Hz. Four MG stations (MG02, 03, 04, and 08) had a locked GPS signal for the duration of the deployment, with well-constrained timing for the entire data collection period, whereas GPS signal was partially unlocked at the remaining four stations (MG01, 05, 06, and 07). The potential time drifts on the four unlocked stations could lead to a failure of codetection. Therefore, timing correction is calculated based on ambient noise cross correlation and applied to those partially unlocked stations. As a result, the absolute time uncertainty at MG01 and 05–07 decreases from  $\sim 1$  to  $\sim 0.1$  s, that is, to negligibly small values (supporting information Figure S1). The timing correction procedure is described in detail in supporting information Text S1 (Bensen et al., 2007; Gou ard et al., 2014; Hable et al., 2018; Hannemann et al., 2013; Lin et al., 2007; Sens-Sch onfelder, 2008; Yao et al., 2011). We use the corrected timing in all the subsequent analysis.

### 2.1. Building an Earthquake Catalog

The construction of an earthquake catalog in this study involves an initial Short-Term-Average/Long-Term-Average (STA/LTA) detection, enhanced by a MMF approach, followed by event location (*Hypocenter*) and relocation (*hypoDD*). We first apply a multistation STA/LTA algorithm (Krischer et al., 2015) to automatically detect 645 initial earthquakes; details of STA/LTA detection method and the parameter choices are introduced in Text S2 (Withers et al., 1998). Since we are primarily interested in the seismicity proximal to the well surrounded by the MG stations ( $\sim 30$  km by 30 km study area marked in Figure 1), we retain the 490 events with S-P time less than 4 s, from which we select MMF templates.

In the next step of MMF detection, we reduce the number of possible templates by using only representative events of distinct families to increase computational efficiency. The 490 events detected by the STA/LTA approach are grouped into 60 families based on the criterion of waveforms correlation coefficient (CC) larger than 0.6 at the (East) horizontal component of MG08, which is the station with the best signal-to-noise ratio (SNR). The event with the highest SNR is then used as the representative template for each family. The MMF method correlates each of the template events in time windows starting 3 s before and after the S arrival (in order to include both P and S phases in the template waveform) on the East components at five stations (MG02, 03, 04, 08, and NBC5). Here we use the East component only, because it has better SNR and performs better in MMF detection than using all three components.

The above procedure results in three hundred 6-s template waveform traces, of which 254 traces with  $\text{SNR} \geq 2$  remain for the MMF detection. Both the templates and continuous waveforms are band-pass filtered between 5 and 15 Hz to aid visual identification of local seismic signals (Walter et al., 2015). We then cross correlate all templates with the continuous waveform at each station and sum the normalized CC values. A detection is declared when the sum exceeds a given threshold, which is usually determined empirically based on the specific tolerance of false detections for a given data set. Here we define a “strong” detection when the summed CC value exceeds 7 times the median absolute deviation ( $7 \cdot \text{MAD}$ ) and a “weak” detection when CC exceeds  $16 \cdot \text{MAD}$  by allowing  $\pm 0.5$ -s shift in the CC calculation to account for colocation tolerance between the template and MMF detections (Peng & Zhao, 2009; Shelly et al., 2007). Further details of the MMF detection method can be found in our previous studies (Wang et al., 2015, 2018).

The automatic strong and weak detections further undergo a visual inspection, using three components of the seismograms recorded at the eight MG stations and NBC5, to remove false detections. Events demonstrating identifiable seismic signals on more than two stations are retained as real detections, resulting in 422 strong and 630 weak detections. It should be noted that the 630 weak detections include the 422 strong detections. In the end, 324 additional events are detected by the MMF method, compared to the original 490



STA/LTA detections. The comparable numbers of detected events using the two methods are due to the fact that the initial STA/LTA detection uses a codetection threshold set as low as 3 in order to include as much seismic signal as possible. Therefore, many seismic signals have already been detected before the application of MMF. However, the total detection of 814 events (Table S2) is a significant improvement over the 28 earthquakes reported for the same time period using only the regional stations (Visser et al., 2017), clearly demonstrating the advantage of dense array coverage.

## 2.2. Event Location and Relocation

We use the program *Hypocenter* (Lienert & Havskov, 1995) to estimate the locations of the 814 detected events, with the origin times estimated from the initial detections and manually picked P and S arrivals. Both the absolute and differential S-P travel times, including data from the four stations with partially unlocked GPS signal, are used (see Text S3 and Figure S2; Klein, 2014; Laske et al., 2013; Lienert & Havskov, 1995; Radke et al., 1982). We also use a larger  $V_P/V_S$  ratio in the top ~3 km than the underlying crystalline crustal materials, to account for the shallow Triassic sedimentary formation in the Montney basin (Laske et al., 2013; Radke et al., 1982). The velocity model used in the inversion is CRUST 1.0 with a  $1^\circ$  by  $1^\circ$  grid centered at ( $57.5^\circ\text{N}$ ,  $122.5^\circ\text{W}$ ), which consists two sedimentary layers with 1- and 1.8-km thickness, overlying the crystalline basement (Laske et al., 2013; Table S1). A total of 558 hypocenters out of the 814 initial detections is constrained by *Hypocenter*.

Of the 558 events, a total of 530 hypocenters is relocated with double-difference relocations (*hypoDD*; Waldhauser, 2001), using the same CRUST 1.0 velocity model. Details of parameter settings are listed in Table S3. We obtain the relocation uncertainty by applying a bootstrap random replacement error estimation based on 100 trials (Waldhauser & Ellsworth, 2000; Yu et al., 2016) and retain 350 of the 530 relocated hypocenters that surpass an error cutoff threshold of 1 and 2 km for horizontal and vertical errors, respectively. Considering the spacing between the five wells in our study area are ~10 km, an epicenter resolution of 1 km is sufficient to spatially correlate earthquakes with individual wells. Table S4 lists the hypocentral information of the 350 relocated events.

## 2.3. Earthquake Distribution and Migration

Figure 2 shows a map of the 350 relocated epicenters, grouped into three clusters. The first cluster (C1) surrounding HF1 commences in close spatial and temporal proximity to the injection stages at the distal end of the well bore and subsequently moves toward the vertical section of the well over the course of injection. Events within the same cluster then migrate from the southern end of the horizontal well bore approximately ~2 km to the south (Figure 3a). In total, 89% (199/223) of events in C1 occurred within the sedimentary layers (hypocentral depths  $\leq 2.8$  km) and 83% (184/223) occurred within 1 km of vertical distance to horizontal section of the wellbore, which ranges from 1.8 to 2.0 km in depth at the northwest and southeast ends, respectively. The second cluster (C2), near station MG08, becomes active at the beginning of the observation period and migrates bilaterally from the center of the cluster. All events in C2 occurred within the sedimentary layers and 78% (39/50) within 1-km vertical distance to the horizontal wellbore of HF1. Although C2 is only approximately 2 km away from HF1, 46% (23/50) of C2 events occurred before the first treatment of HF1, and the remaining 27 events are distributed evenly over the remainder of the 4-month observation period, instead of clustered temporally around HF1 injection. The daily event rate even decreased during HF1 injection period. Cluster 3 (C3) occurs near HF4 and is active simultaneously with HF4 operation, suggesting direct triggering. However, the scattered hypocenters and lack of any migration pattern in C3 may likely be a result of the limited observational capability of the MG network near HF4. We therefore do not attempt to interpret the vertical distribution of events in C3. For the above reasons, we focus on the seismicity migration only of C1 events as they are unambiguously related to injection at HF1.

Liquid-rich gas shale and siltstones in Montney basin result in low diffusivity. However, with the permeability-enhancing treatments, the diffusivity would be increased near HF wells. There is no direct measurement of the hydraulic diffusivity for this area, while seismicity migration pattern is one way to estimate it. The migration pattern revealed by the relocated hypocenters in C1 can be correlated with injection parameters to place constraints on the assumed isotropic hydraulic diffusivity ( $D$ ) for the bulk crustal rock near HF1. We estimate  $D$  for C1 by fitting the epicentral distance ( $r$ ) and occurrence time ( $t$ ) using a diffusional parabolic envelope,  $r = \sqrt{4\pi Dt}$  (Parotidis et al., 2003). Here we assume the origin time and

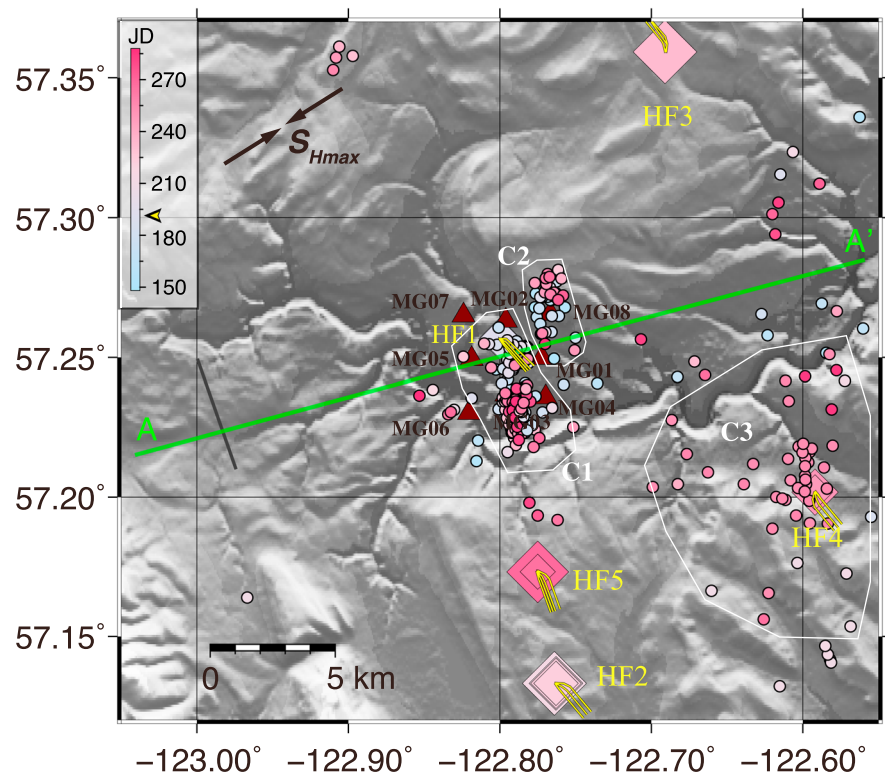


**Figure 2.** Epicenters of double-difference relocated events with horizontal and vertical uncertainties less than 1 and 2 km, respectively (350 in total). Diamonds: hydraulic wells with the same scale as in Figure 1 (size proportional to injection volume), with yellow lines showing map-view projections of horizontal wells. Color bar indicates Julian day in 2015 of event occurrence and well operations (arrow marks the start of HF1 injection). Seismicity clusters are projected onto AA' plane that is approximately parallel to  $S_{Hmax}$  (Bell & Grasby, 2012; projection shown in Figure S3). HF = hydraulic fracturing.

hypo-center of the first detected event following the commencement of HF1 injection as  $r = 0, t = 0$ . We fit the parabolic envelope to the 95th distance percentile in 1-day time bins and estimate the  $D$  value to one significant digit. Figure 3b demonstrates that the preferred value of  $D$  is  $0.2 \text{ m}^2/\text{s}$ . Although the  $D$  value is within the range of typical diffusivity values estimated for the crust ( $0.01\text{--}10 \text{ m}^2/\text{s}$ ; Scholz, 2002), as well as in the estimated range between  $0.1$  and  $2 \text{ m}^2/\text{s}$  of shale gas formations in northwestern Oklahoma (Goebel, Weingarten, et al., 2017), it is higher than typically expected for low-permeability shale and siltstones (Guglielmi et al., 2015). We will discuss the implications of the inferred diffusivity value in section 5.

The projection of all 350 relocated hypocenters along profile AA' indicates events also cluster beneath the HF wells at depths of 0–3 km and at greater depths of 5–18 km (Figure S3). Although the link between the shallow and deep clusters is tenuous due to the limited number of events and the station distribution at the eastern and western edges, it is possible that the deep cluster of events ( $\sim 5\text{--}20 \text{ km}$ ) indicates a steeply dipping ( $\sim 50^\circ$ ) structure with strike direction oriented roughly perpendicular to profile AA', based on a linear-least-squares fit of relocated hypocenters that surpass a relaxed quality control criteria (horizontal and vertical errors both less than 2 km).

### 3. Quantifying Seismicity Correlation to Injection

As shown in Figure 4a, temporal correlations between the detected seismicity and daily injection volumes of the closest wells generally suggest increased seismicity due to injection. In particular, HF1 and HF4 demonstrate strong correlation between injection volume and the number of detected earthquakes, whereas the correlation is not as strong for HF2, HF3, and HF5. In the following, we use a statistical approach to help further establish whether a correlation exists between injection activity and earthquake occurrence.

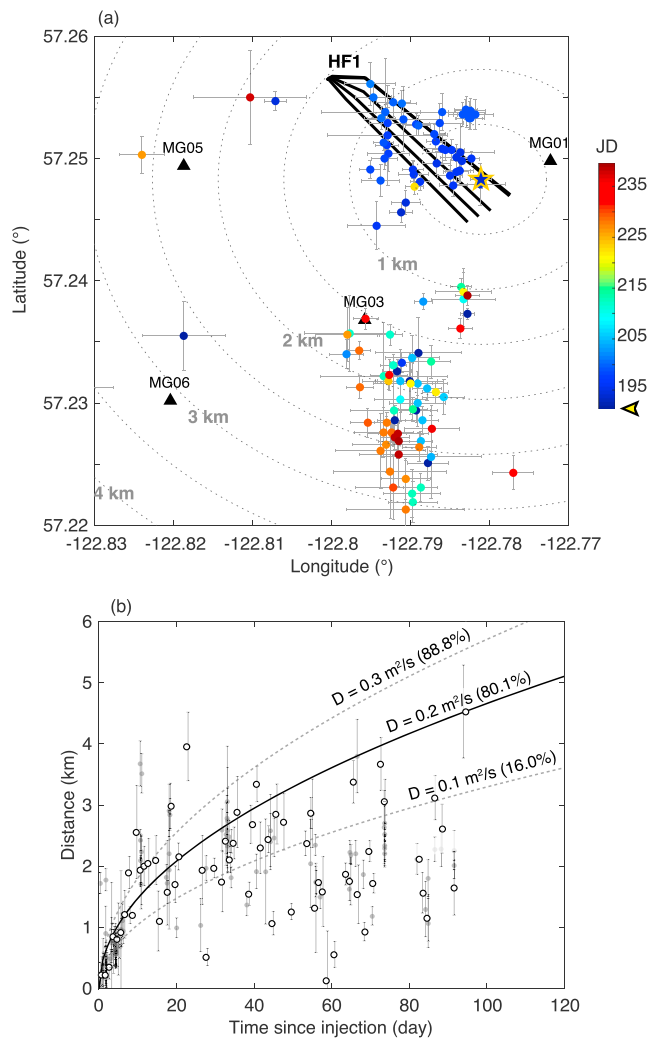


**Figure 3.** (a) Distribution of seismicity in C1 in the 50 days following HF1 injection. Star shows the location of the first detected event after injection, taken as the starting point for earthquake migration. Error bars show the horizontal uncertainties of relocated epicenters. Color bar indicates the Julian date in 2015 of event occurrence, with the yellow arrow marking the start of injection. (b) Seismicity migration of C1, represented by gray dots with location error bars. Open circles are 95th percentile of distance in 1-day time bins. Parabolic envelopes represent the “diffusion front” calculated using different diffusivity values and assuming one pore pressure source for each cluster. The percent of events occurred within the “front” are marked next to each diffusion curve. Solid parabolic envelope indicates preferred diffusivity values  $D = 0.2 \text{ m}^2/\text{s}$ . HF = hydraulic fracturing.

Statistical tests that make assumptions regarding the characteristics of background seismicity are often used to quantify changes in earthquake rates following some stressing event. Here we assume that the stressing event results from the alteration of the subsurface stresses via fluid injection related to HF. The temporal correlation between pumping and changes in earthquake rates can then be quantified using a measure such as the  $\beta$  statistic or some other difference of means test. For example, assuming the earthquake sequence obeys the same Poisson process before and after a stressing event (in our case, onset of injection at a given well), a  $\beta$  statistical value indicates statistical changes in mean seismicity rates by considering the number of events per day before and after the injection. That is, positive  $\beta$  values imply seismicity rate increases, and negative values suggest seismicity rate decreases. A value larger than 2 implies a statistically significant increase in seismicity rate with an implied correlation with the active well (e.g., Matthews & Reasenber, 1988). We also check for a statistical correlation by calculating the Poisson and Gaussian  $p$  values for each injection well and set the triggering threshold at the 95% significance level. A  $p$  value larger than 0.95 indicates strong evidence (at the 95% significance level) against the null hypothesis, thus rejecting the null hypothesis. We test the validity of the assumption that the earthquakes in the (nonclustered) catalog are Poisson ( $\beta$  value and  $p$  value tests) or Gaussian distributed ( $p$  value test), as discussed below. Additionally, we note that we do not use the statistical tests to quantify the magnitude of changes in earthquake rates associated with pumping but only to highlight any potential correlation to pumping at a specific well.

We first find that we cannot reject the null hypothesis that background seismicity is Poisson or Gaussian distributed at the 95% confidence level for both cases. We then use the  $\beta$  value and  $p$  value tests to identify significant changes in background rate following the onset of pumping at HF1–HF5. Figure 1 shows an extended injection history in the study region and demonstrates that injection activity was negligible within the vicinity of HF1–HF5 directly prior to injection at HF1. Therefore, there should be negligible influence of pumping at neighboring wells on the assumed background seismicity rate. Hence, a single background (or prestressing) rate prior to injection at HF1 is used for all five wells. We use “before” and “after” stressing windows of consistent length ranging from 1 to 14 days (discussed below), with the period 1–14 days before injection at HF1 used to estimate the mean background rate. We note that the seismicity rate may deviate from the background distribution following some stressing event (such as well stimulation). Following the reasoning of van der Elst and Brodsky (2010), the difference in average rates prior to and following the stressing event is sufficient to identify a causative trigger (in this case, fluid injection).

Figures 4b–4d shows the correlation with pumping onset at each well (HF1–HF5) using the daily seismicity rate from the catalog (see in Table S2) by computing the Poisson  $\beta$  value and Gaussian  $p$  values, see Text S4 for specific details on the calculations (Matthews & Reasenber, 1988; Wang et al., 2015). We vary the time windows from 1 to 14 days in order to avoid excluding any correlation between delayed seismicity and pumping and show the variation of each statistical measure as a function of the time window length. The  $\beta$  value test (Figure 4b) suggests an increased seismicity rate following injection at wells HF1 and HF4 for time windows exceeding 5 days and at well HF2 for windows exceeding 7 days. The fact that the seismicity rate increase is not significant for shorter time windows may be due to the slow acceleration of injection at the initial stimulation stages, as well as inaccuracy of the reported pumping time (Goebel & Brodsky, 2018).

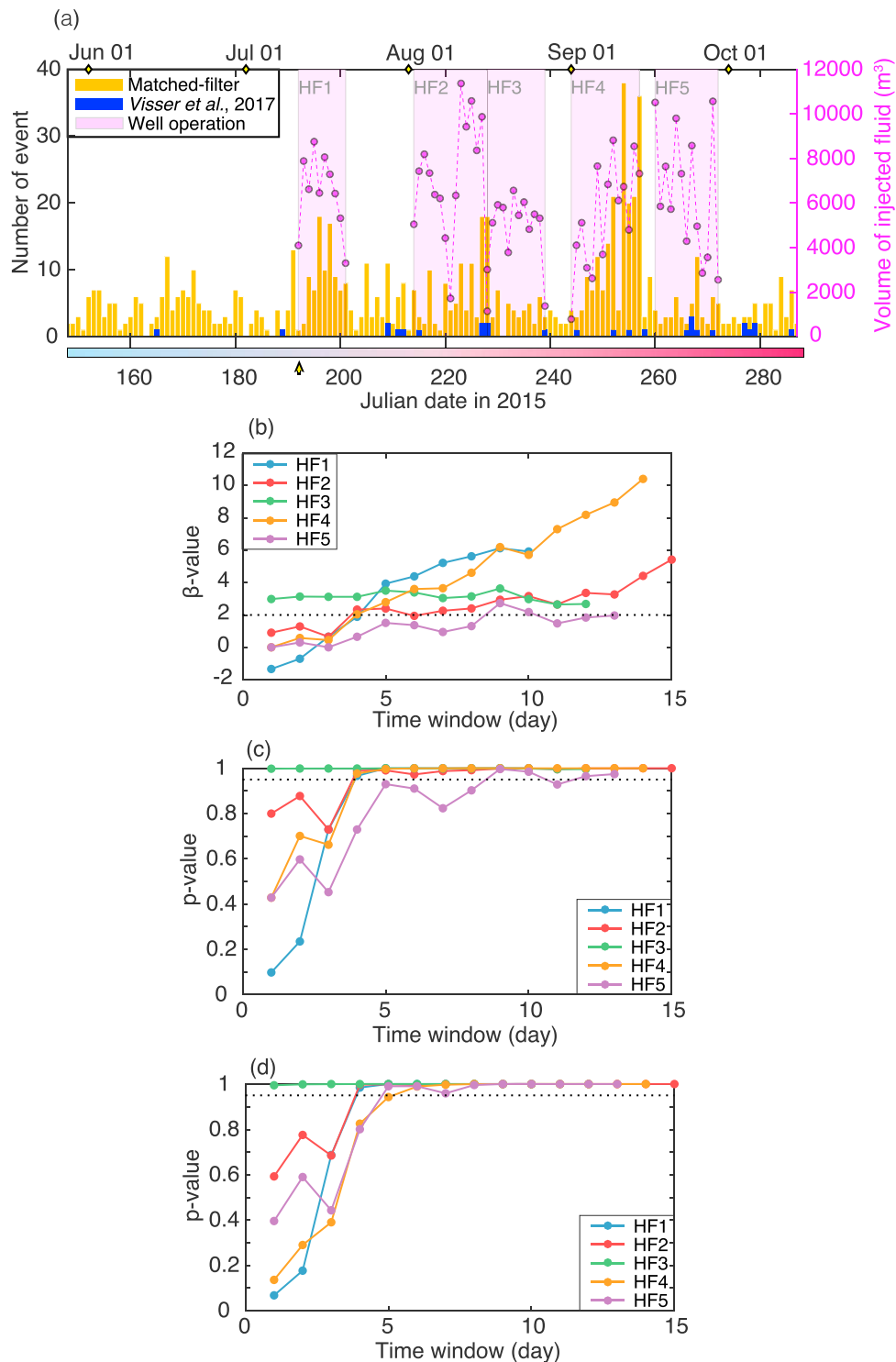


**Figure 4.** (a) Histograms of earthquake catalog and average fluid injection volume. Yellow bars: daily event number of jointly detected by a multistation STA/LTA approach and matched-filter detection in our study area (814 in total). Blue bars: daily event number reported by Visser et al. (2017) of the same area (28 in total). Pink shaded areas: operation periods of five hydraulic fracturing wells (HF1–5) marked in Figure 2. Pink dots: daily injected fluid volume reported by British Columbia Oil and Gas Commission for each well. The Julian date color bar shown in the bottom of the histogram is the same as in Figure 2. (b)  $\beta$  statistical value quantifying changes in seismicity rate due to HF at each well. The x axis shows time-window length dependence on triggering (see Text S4). Background seismicity rate is estimated using events in the same time window before HF1 injection as after injection. Dashed line indicates significance criteria of  $\beta = 2$ . (c) The same as (b) but for the Poisson  $p$  statistic, assuming background seismicity follows a Poisson distribution. The dashed line marks the 95% significance threshold. (d) The same as (c) but under the assumption the background seismicity follows a normal distribution. HF = hydraulic fracturing.

Although the  $\beta$  value is larger than 2 for all the time windows at well HF3, it may be an artifact of increased seismicity at the end of stimulation of HF2. Adding to the ambiguity of the correlation of seismicity increases with HF3 is the fact that there is a 1-day overlap between pumping at HF2 and HF3, and the seismicity rate is low during the remainder of the HF3 injection period (Figure 4a). We also test the null hypothesis that seismicity rate continues to follow the same Poisson or Gaussian distribution after injection commences at HF wells. We can reject the null hypothesis at the 95% level for all distributions, implying a deviation in the seismicity distribution following injection onset. We can also reject the null hypothesis for the time window following injection onset at wells HF1, HF2, and HF4, which is nevertheless consistent with the suggested correlation of seismicity increases with injection activity (Figures 4c and 4d). Well HF5 does not show a significant correlation between injection and seismicity in the  $\beta$  statistic or Poisson  $p$  test and only shows significant changes based on the Gaussian  $p$  test for time windows exceeding 5 days. In summary, the statistical test results suggest that injection at HF1, HF2, and HF4 is correlated with increased rates of local seismicity, while HF3 and HF5 exhibit an ambiguous correlation, at least with our station distribution and resulting catalog.

The statistical tests suggest a temporal correlation between injection and earthquake activity. To show the spatial correlation for each well, we present a comparison of averaged seismicity rates between periods during and outside of injection activity in a circular area of epicentral distance  $<5$  km from each respective well, based on the whole relocated catalog (530 events). Figure S4 demonstrates that all injection wells, with the exception of HF3, are associated with increased seismicity rates at distances less than 5 km, of which HF1 and HF4 have the most pronounced effect.

In order to investigate the effect of pumping on earthquake rates at larger distances, we check the response of earthquake rates within 5 km of HF1, around which the MG network is centered (i.e., where catalog completeness is best), to pumping at wells HF2–HF5. Distances of HF2–HF5 to HF1 range from 9 to 14 km. The daily seismicity rates at HF1 during these pumping periods are all comparable to the background seismicity rate ( $\sim 2$  events per day), indicating that injection at nearby wells has only a negligible effect on earthquake rates at distances larger than  $\sim 10$  km.

We also check the possibility of dynamic triggering by teleseismic earthquakes. As detailed in Text S5 (International Seismological Centre, 2015; Lay & Wallace, 1995; Figure S5), a lack of local events observed in filtered mainshock surface waves coupled with the small estimated peak ground velocity of distant mainshocks ( $<0.01$  cm/s) experienced near the MG array, as well as the statistical results (Figure 4), suggests no significant dynamic triggering occurred during the deployment period.

#### 4. Source Parameter Estimates

Earthquake source parameters, including corner frequency, stress drop, source radius, and seismic moment, provide important information to help understand the physics of fault rupture. While stress drop and source radius are model dependent, the scalar seismic moment  $M_0$  (proportional to earthquake size) and the spectral corner frequency  $f_c$  (inversely proportional to earthquake duration) are two fundamental measurable parameters (e.g., Eshelby, 1957; Hanks & Kanamori, 1979; Haskel, 1969), although  $f_c$  can be difficult to constrain due to influence of attenuation and site response. Earthquakes are empirically observed to have a predictable scaling of  $M_0 \sim f_c^{-3}$  over a broad range of magnitudes, suggesting scale-invariant stress drop values. There are also studies suggesting stress drop increases with moment for smaller magnitudes (e.g., Boatwright, 1994), but it is still an open question as to whether this is an artifact of data processing or has a physical basis, due to difficulties in accounting for nonsource related effects for small amplitude signals (e.g., Ide et al., 2003; Ide & Beroza, 2001; Onwumeka et al., 2018).

We follow the approach of Abercrombie (1995), applying a single-station spectral analysis using waveforms from station MG08, which has the best SNR, to estimate the seismic moment and the spectral corner frequency. We first compute the spectra using a multitaper spectral estimation with the MATLAB PMTM function on time windows of 1 s, starting 0.2 s before the phase arrival, and then fit the spectra using a least-square curve fit. We also compute noise spectra for time windows of the same length ending before the phase arrival for both P and S phases (Figure 5). The fitting method estimates three parameters by fitting a Boatwright model to the displacement spectra of P and S phases: the long period spectral amplitude ( $\Omega_0$ ),



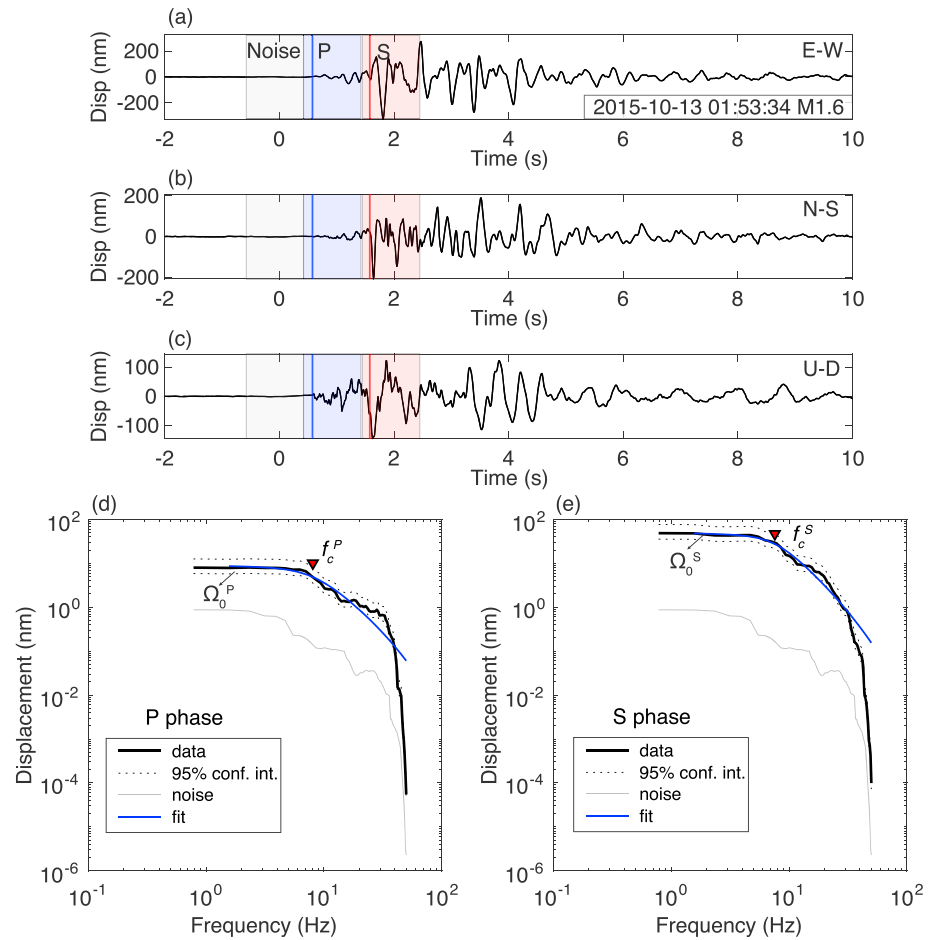


**Figure 5.** A representative example of single spectral fitting. Displacement waveforms of an M1.6 event on 13 October 2015, 01:53:34 recorded at station MG08: (a) E-W, (b) N-S, and (c) vertical components. Gray/blue/pink shaded areas: time windows for obtaining the spectra of noise/P/S phase. The window lengths used are 1 s and start 0.2 s before the phase arrival. (d) Least square curve fits of P phase spectra calculated with a multitaper PMTM function (Prieto, Thomson, et al., 2007; Prieto, Parker, et al., 2007). The fitting only applies to the frequencies within which signal-to-noise ratio > 2. The inverted triangle marks the fitted corner frequency. The long period spectral amplitude ( $\Omega_0$ ) is estimated via averaging the five lowest fitted frequency data points. (e) The same as the left panel for the S phase.

the spectral corner frequency ( $f_c$ ), and high-frequency falloff rate on a log-log plot ( $n$ ). The analytical form of the displacement spectrum is given by the following equation (Boatwright, 1980):

$$\Omega(f) = \Omega_0 \frac{e^{-(\pi f t / Q)}}{[1 + (f/f_c)^{2n}]^{1/2}}, \quad (1)$$

where  $t$  is travel time, and  $Q$  is a quality factor assumed to be 1,000. The values of  $\Omega_0$  and  $f_c$  subsequently provide estimates of seismic moment ( $M_0$ ), source radius ( $r$ ), and stress drop ( $\Delta\sigma$ ) using the following equations with a circular crack model (Aki & Richards, 1980; Brune, 1970, 1971; Eshelby, 1957; Madariaga, 1976):

$$M_0 = \frac{4\pi\rho c^3 R \Omega_0}{U_{\phi\theta}}, \quad (2)$$

$$r = \frac{3kc_s}{f_c}, \quad (3)$$

$$\Delta\sigma = \frac{7M_0}{16r^3}, \quad (4)$$

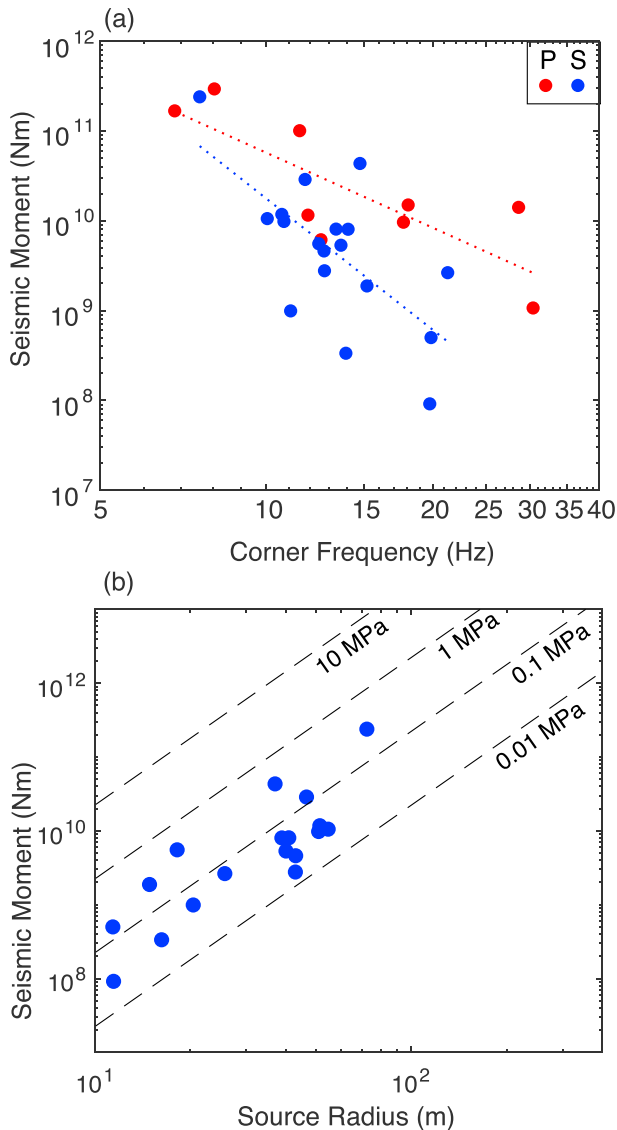


**Figure 6.** (a) Scaling between corner frequency  $f_c$  and seismic moment  $M_0$ . Red/blue solid dots:  $f_c$  and  $M_0$  estimated based on the single spectral fitting of P/S phase. The best-fit scaling relations are  $\log_{10}(M_0^P) = -2.77 \log_{10}(f_c^P) + 13.53$  and  $\log_{10}(M_0^S) = -4.85 \log_{10}(f_c^S) + 15.09$ , for P and S phases, respectively. (b) Seismic moment versus source radius. Both quantities are estimated from the single spectral fitting of S phases. The scaling for the P phases is shown in Figure S8.

where the density,  $\rho$ , is set at  $2,790 \text{ kg/m}^3$ , velocity  $c$  for P and S waves is chosen at the hypocentral depth (Table S1), and  $R$  is the hypocentral distance. The mean radiation pattern,  $U_{\phi\theta}$ , is set to be 0.52 and 0.63 for P and S waves, respectively (Aki & Richards, 1980), and  $k$ , a constant related to the reciprocal relation between  $f_c$  and  $r$ , is set as 0.32 and 0.21 for P and S waves, respectively (Madariaga, 1976). It should be noted that the expressions and constants in equations (1)–(4) may differ among models (e.g., Brune, 1970, 1971; Boatwright, 1980). Thus, the relative values we obtain are indicative of scaling, but any attempt to compare absolute values across studies should always consider the specific type of source model and assumed constants.

We estimate the moment and corner frequency values by fitting the individual source spectra using equation (1) (representative examples show in Figure S6). Figure S7 shows the estimated corner frequency values. The range of estimated  $f_c$  values for the induced events is 7–30 Hz, and the ratio of corner frequency values determined for P and S phases ( $f_c^P/f_c^S$ ) is 1.31. As shown in Figure 6a, the fitted slopes for the relation between corner frequency and seismic moment based on P and S phases show obvious differences between the P-phase fitting ( $-2.77$ ) and the S-phase fitting ( $-4.85$ ). The estimated source radius for the induced events ranges from  $\sim 10$  to  $100 \text{ m}$ , with seismic moment between  $\sim 10^8$  and  $10^{11} \text{ Nm}$ , implying stress drop values of 0.01 to 1 MPa (Figures 6b and S8). We note that corner frequencies of events with seismic moment smaller than  $\sim 10^{10} \text{ Nm}$  become difficult to constrain with surface stations and single spectrum estimates; stress drop error bars generally increase with the decreasing event magnitudes. Thus, the estimated scaling should be interpreted with caution for events of  $M_0 < \sim 10^{10} \text{ Nm}$ .

In addition, we use amplitude ratios to estimate the seismic moment values of smaller events detected by the MMF that did not have enough phase arrivals to be reliably located, based on the relation  $M_0 \propto R\Omega_0$  (equation (2)). Following van der Elst et al. (2013), we calculate three-component displacement waveforms of earthquakes with clear signals ( $\text{SNR} \geq 2$ ) after applying an 8-Hz high-pass filter and measure the peak amplitude within a 4-s window starting at the S wave arrival. Every order of station-averaged amplitude difference between a template and another strong detection corresponds to one unit of difference in magnitude. We estimate the magnitudes of 422 strong detections using their amplitude ratios to collocated template events with calculated seismic moment from individual spectra. As Figure S9a shows, including the estimated magnitudes of the MMF detection extends the range of catalog magnitudes from  $\sim M-2.8$  to  $\sim M1.8$ . Note that larger events ( $M > 1$ ) occur nearly exclusively during injection periods. The magnitude-frequency distribution indicates

a magnitude completeness of  $M_c \sim -0.2$  for the catalog created here (Figure S9b; Wiemer & Wyss, 2000). We estimate a corresponding  $b$  value of  $0.84 \pm 0.09$  based on a maximum-likelihood method (Aki, 1965; Shi & Bolt, 1982).

## 5. Discussion

Figures 2 and 4 demonstrate a strong temporal and spatial ( $< 5 \text{ km}$ ) correlation between induced seismicity and fluid injection, particularly near wells HF1 and HF4. Figure 3 shows that while seismicity migrates with increasing time away from the well bore, some earthquakes also occur at distances up to  $\sim 3\text{--}4 \text{ km}$  at short time scales after injection starts, which begs the question as to whether pore pressure diffusion or poroelasticity of the rock matrix dominates the injection-induced stress transfer.

Seismic cluster C1 near HF1 follows a diffusive migration pattern that is well described by a square-root envelope (with 80.1% of events following the estimated diffusivity), suggesting pore pressure diffusion (Goebel & Brodsky, 2018; Segall & Lu, 2015). Another factor supporting pore pressure diffusion as a means of stress transfer is that earthquake rates are positively correlated with the cumulative sum of injection volume during the HF treatment (Figure 4a), which could be related to the pressure increase caused by fluid diffusion (Huang & Beroza, 2015; van der Elst et al., 2013). Such an argument is also supported by the study of Schultz et al. (2018) in the Duvernay play (Alberta, Canada), suggesting a linear scaling between injection volume and seismic productivity (event count). Alternatively, induced seismicity controlled by poroelastic stress change, without a characteristic delay from fluid diffusion, would be potentially more sensitive to the pumping rate (e.g., Goebel, Weingarten, et al., 2017), rather than the total volume. Here we only have information about the daily average pumping rate, which precludes us from correlating seismicity rate with the maximum pumping rate. We can therefore only make limited inferences with respect to poroelastic stress transfer based on pumping rate data.

Lithology may also have important implications for poroelastic stress transfer. For example, the maximum injection depth at HF1 is  $\sim 1.9$  km, within the sedimentary layers (0–2.8 km) and roughly 1 km above the basement contact. (Note that the horizontal well bore is not level but dips with the Montney Formation, thus ranges in depth from approximately 1.8–2.0 km). Goebel and Brodsky (2018) point out that the bulk strain in soft sedimentary rocks is more strongly coupled to pore fluid volume changes (which could originate from fluid injection) compared to the crystalline basement. Thus, stress perturbations from pumping may be transmitted more dominantly via poroelastic stress transfer compared to the basement rock units with a lower Biot coefficient. Given that injection occurs around HF1 in the sedimentary layers where strong poroelastic coupling is expected, we perform a consistency check on the seemingly contradictory hypothesis that pore pressure diffusion dominates stress transfer in the context of the estimated diffusivity values. We use a simple poroelastic model to calculate the spatiotemporal evolution of solid matrix stresses and pore pressure changes due to successive point-source injections (Figure S10). The aim of the model is to check, to first order, if pore pressure stresses dominate within 5 km of the well bore of HF1, or whether poroelastic stresses are needed to explain the distribution of seismicity within the sedimentary layers. We use the program POEL (Wang & Kumpel, 2003) to model a layered elastic medium inferred from Crust 1.0 (Laske et al., 2013), with inputs from the daily injection volumes at HF1 (Figure S10b), and our estimated diffusivity value of  $0.2 \text{ m}^2/\text{s}$ . We assume the confining pressure of the shale unit undergoing injection is approximately  $\sim 50$  MPa and set the Biot coefficient value  $\alpha = 0.5$  for the two overlying sedimentary layers, according to Gutierrez et al. (2015), and use a value of  $\alpha = 0.2$  for the basement layer (Detournay & Cheng, 1993). We also set the undrained Skempton coefficient  $B$  (the change in pore pressure per unit change in confining pressure) as 0.75 (Deng et al., 2016). The collocated point injection sources (neglecting lateral spread) are located at a depth of 1.9 km (Figure S10a), the average depth of the horizontal portion of the well bore. Text S6 provides details of the model calculation (Deng et al., 2016; Detournay & Cheng, 1993; Gutierrez et al., 2015; Laske et al., 2013; Rice & Cleary, 1976; Skempton, 1954; Wang & Kumpel, 2003).

Each panel in Figure 7 shows the evolution of the calculated pore pressure and (radial) poroelastic stress values at the depth of 1.9 km at successively greater distances ( $r = 1\text{-km}$  intervals) to the well, compared to seismicity within 100 days of injection onset. The radial stress ( $\Delta\sigma_{rr}$ ) is plotted for comparison to pore pressure ( $\Delta P_p$ ), as its amplitude is an order of magnitude larger than all other stress tensor components. Here we define tension to be positive. Figure 7 demonstrates that at all distances considered,  $\Delta\sigma_{rr}$  declines briefly as the pumping starts and remains compressive prior to the arrival of fluid diffusion front, as inferred by the increasing and high pore pressure values ( $\Delta P_p$ ). Once the fluid diffusion front passes,  $\Delta\sigma_{rr}$  changes from compression to tension (negative to positive values). After a characteristic period ( $t \sim r^2/D$ ; Parotidis et al., 2003), both  $\Delta P_p$  and  $\Delta\sigma_{rr}$  approach zero. We note that the evolution of  $\Delta P_p$  and  $\Delta\sigma_{rr}$  does not change significantly when using a higher  $\alpha$  value ( $=1$ ) for the sedimentary layers while keeping a constant  $\alpha = 0.2$  in the basement layer. We also note that the calculation in the near field ( $r < 200$  m) may not be valid due to the high and largely unconstrained permeability-enhancement resulting from fracture formation during the HF treatment. Events at such small distances likely result from stresses applied directly to the rock framework through hydraulic stimulation (Zeng et al., 2014).

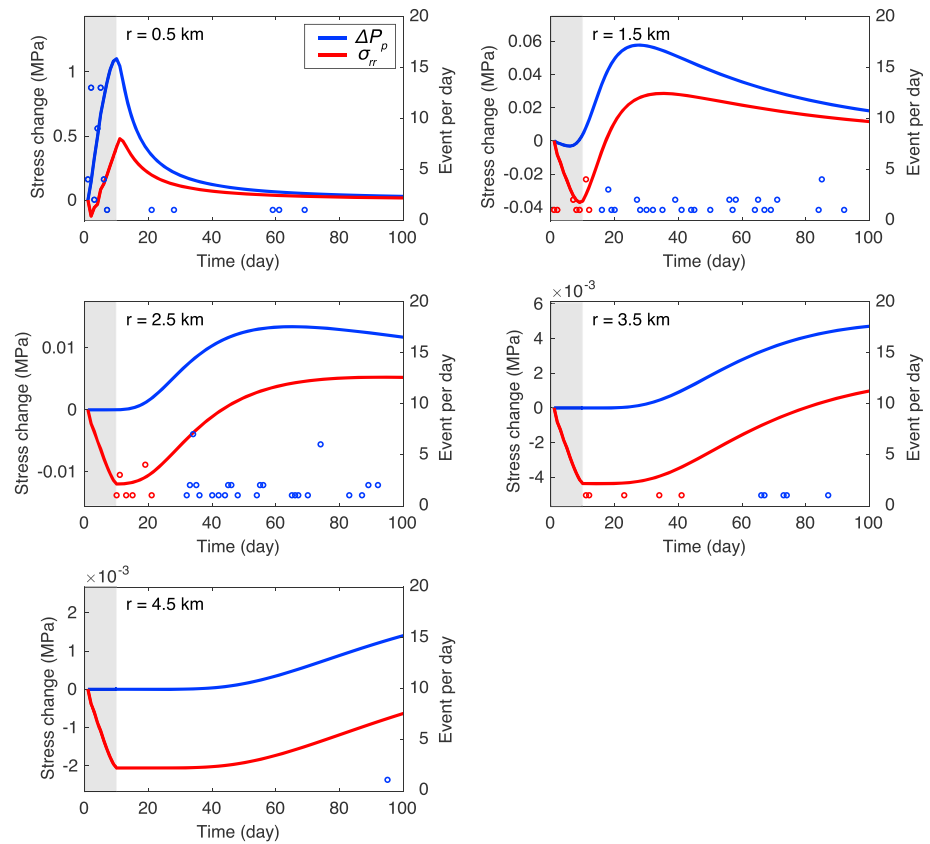


**Figure 7.** Evolution of excess pore pressure (blue) and poroelastic stress change (red) due to fluid injection at hydraulic fracturing 1, at the injection point depth (1.9 km) with radial distances of (a) 0.5, (b) 1.5, (c) 2.5, (d) 3.5, and (e) 4.5 km to hydraulic fracturing 1. Blue/red dots are the daily number of earthquakes that located within each distance range of  $\pm 0.5$  km and occurred after/before the arrival of the fluid diffusion front, suggesting a dominant mechanism of pore pressure increase/poroelastic stress transfer. The shaded area indicates the 10-day injection period.

Comparing the stress evolution to the pattern of seismicity suggests that (1)  $\Delta P_p$  has a dominant effect on the number of earthquakes at distances  $< 1$  km (Figure 7a) and (2) poroelastic stress transfer,  $\Delta \sigma_{rr}$ , may more readily explain the occurrence of earthquakes before the fluid diffusion front passes at intermediate distances of  $\sim 1$ – $4$  km (Figures 7b–7d). According to our model, both pore pressure diffusion and poroelastic stress change influence the process of stress transfer, thus the seismicity distribution, after the fluid diffusion front passes by. We note that the radially compressive/tensile stress change here could possibly cause a large value of shear stress change on a specific fault orientation; identifying the relative influence of the two mechanisms would require taking the fault orientation into consideration. However, as stated above, the model is intended as more of a consistency check on the plausibility of pore pressure dominating stress transfer at short distances, instead of triggering mechanism for individual seismicity or seismicity clusters. Both the model and Figure 3 suggest pore pressure may dominate at distances of  $< 1$  km, while poroelastic stresses may also be important at greater distances, even still within 5 km of the wellbore.

It is also important to consider the possibility of a hydraulic connection. That is, fluid movement and pore pressure evolution can be channeled through faults or other structural conduits with high permeability. As noted above, the hydraulic diffusivity of  $\sim 0.2$  m<sup>2</sup>/s estimated from the seismicity migration pattern is much higher than typical expected values of shale formations (e.g.,  $\sim 10^{-9}$  m<sup>2</sup>/s reported by Guglielmi et al., 2015), suggesting the earthquakes in C1 might have migrated along a fault acting as a fluid conduit (Caine et al., 1996). To first order, the migration pattern of C1 strikes roughly consistent with a geological fabric (fault) that is perpendicular to the regional maximum horizontal compression  $S_{Hmax}$  (Figure 2). In addition, the seismic  $b$  value of  $0.84 \pm 0.09$  implies events nucleate on a well-developed fault with smooth surfaces capable of hosting large ruptures (Goebel, Kwiatak, et al., 2017; Kozłowska et al., 2018), which would also be



consistent of fault-parallel conduit behavior. A hydraulic conduit could also connect to the basement (Galloway et al., 2018). If such a structure exists, one should expect seismicity in the basement to follow pore pressure diffusive character due to the expected lower Biot coefficient value there (Goebel & Brodsky, 2018). The 23 earthquakes of C1 located at basement depths (Figure S10a) could indicate hydraulic communication with basement-rooted faults. However, the majority of seismicity occurs within the sedimentary layers, suggesting that much of the fluid movement occurs within them. Alternatively, although the radial diffusion is an oversimplification for a hydraulic connection, the presence of such a high-permeability conduit would only increase pore pressure on structure(s) of a dimension comparable to the cross-sectional area of the conduit, as demonstrated in a fully coupled poroelastic stress model with anisotropic permeability (Deng et al., 2016). Therefore, it would not change the interpretation of the relative importance of pore pressure versus poroelastic stress transfer within the structural conduit of high-permeability as opposed to isotropic fluid migration.

Figure 6a suggests some preliminary evidence for seismic anisotropy through the difference in corner frequency scaling between P and S phases that would also be consistent with a distinct orientation of fault/crack geometry. In other words, the different moment-duration scaling between P and S phases of high-frequency events may result from path effects on shear waves caused by anisotropy dictated by the travel path from source to receiver. More robust moment-duration scaling obtained from spectral ratio fitting with the full set of high-frequency events will follow in future work to further explore the effect of anisotropy. In addition, shear wave splitting analysis (e.g., Cochran et al., 2003) will help confirm whether the anisotropy is due to cracks induced by the fluid injection or from preexisting structures.

## 6. Conclusions

Here we present a detailed study of earthquakes associated with a HF stimulation in the Montney basin of northeast British Columbia, Canada, capturing events prior to, during, as well as the decay in seismicity after injection ceased. Using new data from a temporary deployment of eight broadband stations centered within 3 km of the HF well, we establish temporal and spatial correlations of 350 well-located events to the HF treatment at the target well and one of four additional surrounding wells. The migration pattern of induced earthquakes within 5 km of the target well implies crustal diffusivity values of  $\sim 0.2 \text{ m}^2/\text{s}$ , suggesting that pore pressure diffusion is a viable mechanism for triggering at distances of up to 1 km, whereas poroelastic stresses are needed to explain the distribution of earthquakes at distances up to 4 km, at least on time scales shorter than fluid diffusion. Both pore pressure diffusion and poroelastic stress seem to have limited effects on transferring substantial stress perturbations to induce earthquakes at distance larger than 5 km in our study area.

### Acknowledgments

We thank Gail Atkinson, an anonymous reviewer, and the Associate Editor for their comments that helped to improve this manuscript. We thank Conan Drummond for his help in the deployment of seismic stations, as well as Progress Energy, in particular, Mark Norton, for assistance in collecting the waveform data and The BC Oil and Gas Commission for providing injection data. We also thank Huajian Yao for sharing the Ambient noise cross-correlation codes for daily long SAC format data (<http://yaolab.ustc.edu.cn/resources.php?i=28>). This work is supported in part by an NSERC Discovery Grant, and start-up funds from the Ruhr University Bochum. Waveforms of the 350 events listed in Table S4 can be downloaded online ([https://www.geophysik.ruhr-uni-bochum.de/download/public/event\\_waveform\\_sac.zip](https://www.geophysik.ruhr-uni-bochum.de/download/public/event_waveform_sac.zip)).

### References

- Abercrombie, R. E. (1995). Earthquake source scaling relationships from  $-1$  to  $5 M_L$  using seismograms recorded at 2.5-km depth. *Journal of Geophysical Research*, *100*(B12), 24,015–24,036.
- Aki, K. (1965). Maximum likelihood estimate of  $b$  in the formula  $\log N = a - bM$  and its confidence limits. *Bulletin of the Earthquake Research Institute, Tokyo University*, *43*, 237–239.
- Aki, K., & Richards, P. (1980). *Quantitative seismology* (p. 932). New York: W. H. Freeman.
- Altmann, J. B., Heidbach, O., & Gritto, R. (2013). Relative importance of processes leading to stress changes in the Geysers geothermal area. In *Proceedings of thirty-eighth workshop on geothermal reservoir engineering*. Stanford, CA: Stanford Geothermal Program.
- Atkinson, G. M., Eaton, D. W., Ghofrani, H., Walker, D., Cheadle, B., Schultz, R., et al. (2016). Hydraulic fracturing and seismicity in the Western Canada Sedimentary Basin. *Seismological Research Letters*, *87*(3), 631–647.
- BC Oil and Gas Commission (2012). *Investigation of observed seismicity in the Horn River Basin*. British Columbia, Canada: BC Oil and Gas Commission. Retrieved from <https://www.bcogc.ca/investigation-observed-seismicity-horn-river-basin>
- Bell, J. S., & Grasby, S. E. (2012). The stress regime of the Western Canadian sedimentary basin. *Geofluids*, *12*(2), 150–165.
- Bensen, G. D., Ritzwoller, M. H., Barmin, M. P., Levshin, A. L., Lin, F., Moschetti, M. P., et al. (2007). Processing seismic ambient noise data to obtain reliable broad-band surface wave dispersion measurements. *Geophysical Journal International*, *169*(3), 1239–1260. <https://doi.org/10.1111/j.1365-246X.2007.03374.x>
- Boatwright, J. (1980). A spectral theory for circular seismic sources; simple estimates of source dimension, dynamic stress drop, and radiated seismic energy. *Bulletin of the Seismological Society of America*, *70*(1), 1–27.
- Boatwright, J. (1994). Regional propagation characteristics and source parameters of earthquakes in Eastern North America. *Bulletin of the Seismological Society of America*, *84*, 1–15.
- Brune, J. N. (1970). Tectonic stress and seismic shear waves from earthquakes. *Journal of Geophysical Research*, *75*, 4997–5009.
- Brune, J. N. (1971). Seismic sources fault plane studies and tectonics. *Eos, Transactions American Geophysical Union*, *52*(5), IUGG178–IUGG 187. <https://doi.org/10.1029/EO052i005pIUGG178>

- Caine, J. S., Evans, J. P., & Forster, C. B. (1996). Fault zone architecture and permeability structure. *Geology*, *24*(11), 1025–1028.
- Clarke, H., Eisner, L., Styles, P., & Turner, P. (2014). Felt seismicity associated with shale gas hydraulic fracturing: The first documented example in Europe. *Geophysical Research Letters*, *41*, 8308–8314. <https://doi.org/10.1002/2014GL062047>
- Cochran, E. S., Vidale, J. E., & Li, Y.-G. (2003). Near-fault anisotropy following the Hector Mine earthquake. *Journal of Geophysical Research*, *108*(B9), 2436. <https://doi.org/10.1029/2002JB002352>
- Deng, K., Liu, Y., & Harrington, R. M. (2016). Poroelastic stress triggering of the December 2013 Crooked Lake, Alberta, induced seismicity sequence. *Geophysical Research Letters*, *43*, 8482–8491. <https://doi.org/10.1002/2016GL070421>
- Detournay, E., & Cheng, A. H.-D. (1993). Fundamentals of poroelasticity. In C. Fairhurst (Ed.), *Comprehensive rock engineering: Principles, practice and projects, Vol. II, Analysis and Design Method* (pp. 113–171). Oxford, UK: Pergamon Press.
- Ellsworth, W. L. (2013). Injection-induced earthquakes. *Science*, *341*(6142), 1225–1229.
- Eshelby, J. D. (1957). The determination of the elastic field of an ellipsoidal inclusion, and related problems. *Proceedings of the Royal Society of London A*, *241*(1226), 376–396.
- Galloway, E., Hauck, T., Corlett, H., Paná, D., & Schultz, R. (2018). Faults and associated karst collapse suggest conduits for fluid-flow that influence hydraulic fracturing induced seismicity. *Proceedings of the National Academy of Sciences*, *115*(43), E10003–E10012.
- Goebel, T. H. W., & Brodsky, E. E. (2018). The spatial footprint of injection wells in a global compilation of induced earthquake sequences. *Science*, *361*(6405), 899–904.
- Goebel, T. H. W., Hosseini, S. M., Cappa, F., Hauksson, E., Ampuero, J. P., Aminzadeh, F., & Saleeby, J. B. (2016). Wastewater disposal and earthquake swarm activity at the southern end of the Central Valley, California. *Geophysical Research Letters*, *43*, 1092–1099. <https://doi.org/10.1002/2015GL066948>
- Goebel, T. H. W., Kwiatek, G., Becker, T. W., Brodsky, E. E., & Dresen, G. (2017). What allows seismic events to grow big?: Insights from b-value and fault roughness analysis in laboratory stick-slip experiments. *Geology*, *45*(9), 815–818.
- Goebel, T. H. W., Weingarten, M., Chen, X., Haffener, J., & Brodsky, E. E. (2017). The 2016  $M_w$ 5.1 Fairview, Oklahoma earthquakes: Evidence for long-range poroelastic triggering at >40 km from fluid disposal wells. *Earth and Planetary Science Letters*, *472*, 50–61.
- Gouédard, P., Seher, T., McGuire, J. J., Collins, J. A., & van der Hilst, R. D. (2014). Correction of ocean-bottom seismometer instrumental clock errors using ambient seismic noise. *Bulletin of the Seismological Society of America*, *104*(3), 1276–1288.
- Guglielmi, Y., Ellsworth, D., Cappa, F., Henry, P., Gout, C., Dick, P., & Durand, J. (2015). In situ observations on the coupling between hydraulic diffusivity and displacements during fault reactivation in shales. *Journal of Geophysical Research: Solid Earth*, *120*, 7729–7748. <https://doi.org/10.1002/2015JB012158>
- Gutierrez, M., Katsuki, D., & Tutuncu, A. (2015). Determination of the continuous stress-dependent permeability, compressibility and poroelasticity of shale. *Marine and Petroleum Geology*, *68*, 614–628.
- Hable, S., Sigloch, K., Barruol, G., Stähler, S. C., & Hadziioannou, C. (2018). Clock errors in land and ocean bottom seismograms: High-accuracy estimates from multiple-component noise cross-correlations. *Geophysical Journal International*, *214*, 2014–2034.
- Hanks, T. C., & Kanamori, H. (1979). Moment magnitude scale. *Journal of Geophysical Research*, *84*, 2348–2350.
- Hannemann, K., Krüger, F., & Dahm, T. (2013). Measuring of clock drift rates and static time offsets of ocean bottom stations by means of ambient noise. *Geophysical Journal International*, *196*(2), 1034–1042.
- Haskel, B. G. (1969). External events and internal appraisals: A note on the proposed Nordic common market. *International Organization*, *23*(4), 960–968.
- Healy, J. H., Rubey, W. W., Griggs, D. T., & Rayleigh, C. B. (1968). The Denver earthquakes. *Science*, *161*, 1301–1310.
- Holland, A. (2013). Earthquakes triggered by hydraulic fracturing in south-central Oklahoma. *Bulletin of the Seismological Society of America*, *103*, 1784–1792. <https://doi.org/10.1785/0120120109>
- Horton, S. (2012). Disposal of hydrofracking waste fluid by injection into subsurface aquifers triggers earthquake swarm in central Arkansas with potential for damaging earthquake. *Seismological Research Letters*, *83*(2), 250–260.
- Hsieh, P. A., & Bredehoeft, J. D. (1981). A reservoir analysis of the Denver earthquakes: A case of induced seismicity. *Journal of Geophysical Research*, *86*(B2), 903–920.
- Huang, Y., & Beroza, G. C. (2015). Temporal variation in the magnitude-frequency distribution during the Guy-Greenbrier earthquake sequence. *Geophysical Research Letters*, *42*, 6639–6646. <https://doi.org/10.1002/2015GL065170>
- Ide, S., & Beroza, G. C. (2001). Does apparent stress vary with earthquake size? *Geophysical Research Letters*, *28*(17), 3349–3352.
- Ide, S., Beroza, G. C., Prejane, S. G., & Ellsworth, W. L. (2003). Apparent break in earthquake scaling due to path and site effects on deep borehole recordings. *Journal of Geophysical Research*, *108*(B5), 2271. <https://doi.org/10.1029/2001JB001617>
- International Seismological Centre (2015). On-line Bulletin. Thatcham, UK: International Seismology Centre. <http://www.isc.ac.uk>
- International Seismological Centre (2019). On-line Bulletin. Thatcham, UK: International Seismology Centre. <http://www.isc.ac.uk>
- Keranen, K., Weingarten, M., Abers, G., Bekins, B., & Ge, S. (2014). Sharp increase in central Oklahoma seismicity since 2008 induced by massive wastewater injection. *Science*, *345*(6195), 448–451.
- Keranen, K. M., Savage, H. M., Abers, G. A., & Cochran, E. S. (2013). Potentially induced earthquakes in Oklahoma, USA: Links between wastewater injection and the 2011  $M_w$  5.7 earthquake sequence. *Geology*, *41*(6), 699–702.
- Klein, F. W. (2014). *User's guide to HYPOINVERSE-2000, a Fortran Program to solve for earthquake locations and magnitudes* (US Geological Survey Open File Report 02-171, Version 1.40). Menlo Park, CA: U.S. Geological Survey.
- Kozłowska, M., Brudzinski, M. R., Friberg, P., Skoumal, R. J., Baxter, N. D., & Currie, B. S. (2018). Maturity of nearby faults influences seismic hazard from hydraulic fracturing. *Proceedings of the National Academy of Sciences*, *115*(8), E1720–E1729.
- Krischer, L., Megies, T., Barsch, R., Beyreuther, M., Lecocq, T., Caudron, C., & Wassermann, J. (2015). ObsPy: A bridge for seismology into the scientific Python ecosystem. *Computational Science & Discovery*, *8*(1), 014003. <https://doi.org/10.1088/1749-4699/8/1/014003>
- Laske, G., Masters, G., Ma, Z., & Pasyanos, M. (2013). *Update on CRUST1.0—A 1-degree global model of Earth's crust*. *Geophysical Research Abstracts* *15*, Abstract EGU2013-2658.
- Lay, T., & Wallace, T. C. (1995). *Modern global seismology* (Vol. 5). Waltham, MA: Academic Press.
- Lei, X., Huang, D., Su, J., Jiang, G., Wang, X., Wang, H., et al. (2017). Fault reactivation and earthquakes with magnitudes of up to  $M_w$  4.7 induced by shale-gas hydraulic fracturing in Sichuan Basin, China. *Scientific Reports*, *7*(1), 7971.
- Lienert, B. R. E., & Havskov, J. (1995). A computer program for locating earthquakes both locally and globally. *Seismological Research Letters*, *66*, 26–36.
- Lin, F. C., Ritzwoller, M. H., Townend, J., Bannister, S., & Savage, M. K. (2007). Ambient noise Rayleigh wave tomography of New Zealand. *Geophysical Journal International*, *170*(2), 649–666.

- Madariaga, R. (1976). Dynamics of an expanding circular fault. *Bulletin of the Seismological Society of America*, 66, 639–666.
- Mahani, A. B., Schultz, R., Kao, H., Walker, D., Johnson, J., & Salas, C. (2017). Fluid injection and seismic activity in the northern Montney play, British Columbia, Canada, with special reference to the 17 August 2015 Mw 4.6 induced earthquake. *Bulletin of the Seismological Society of America*, 107(2), 542–552.
- Martínez-Garzón, P., Kwiatek, G., Sone, H., Bohnhoff, M., Dresen, G., & Hartline, C. (2014). Spatiotemporal changes, faulting regimes, and source parameters of induced seismicity: A case study from the Geysers Geothermal Field. *Journal of Geophysical Research: Solid Earth*, 119, 8378–8396. <https://doi.org/10.1002/2014JB011385>
- Matthews, M. V., & Reasenber, P. A. (1988). Statistical-methods for investigating quiescence and other temporal seismicity patterns. *Pure and Applied Geophysics*, 126(2–4), 357–372. <https://doi.org/10.1007/Bf00879003>
- Onwuemeka, J., Liu, Y., & Harrington, R. M. (2018). Earthquake stress drop in the Charlevoix Seismic Zone, eastern Canada. *Geophysical Research Letters*, 45, 12,226–12,235. <https://doi.org/10.1029/2018GL079382>
- Parotidis, M., Rothert, E., & Shapiro, S. A. (2003). Pore-pressure diffusion: A possible triggering mechanism for the earthquake swarms 2000 in Vogtland/NW-Bohemia, central Europe. *Geophysical Research Letters*, 30(20), 2075. <https://doi.org/10.1029/2003GL018110>
- Peng, Z., & Zhao, P. (2009). Migration of early aftershocks following the 2004 Parkfield earthquake. *Nature Geoscience*, 2(12), 877–881. <https://doi.org/10.1038/ngeo697>
- Prieto, G. A., Parker, R. L., Thomson, D. J., Vernon, F. L., & Graham, R. L. (2007). Reducing the bias of multitaper spectrum estimates. *Geophysical Journal International*, 171(3), 1269–1281. <https://doi.org/10.1111/j.1365-246X.2007.03592.x>
- Prieto, G. A., Thomson, D. J., Vernon, F. L., Shearer, P. M., & Parker, R. L. (2007). Confidence intervals for earthquake source parameters. *Geophysical Journal International*, 168(3), 1227–1234. <https://doi.org/10.1111/j.1365-246X.2006.03257.x>
- Radke, M., Welte, D. H., & Willsch, H. (1982). Geochemical study on a well in the Western Canada Basin: Relation of the aromatic distribution pattern to maturity of organic matter. *Geochimica et Cosmochimica Acta*, 46(1), 1–10. [https://doi.org/10.1016/0016-7037\(82\)90285-X](https://doi.org/10.1016/0016-7037(82)90285-X)
- Rayleigh, C. B., Healy, J. H., & Bredehoeft, J. D. (1976). An experiment in earthquake control at Rangely, Colorado. *Science*, 191(4233), 1230–1237. <https://doi.org/10.1126/science.191.4233.1230>
- Rice, J. R., & Cleary, M. P. (1976). Some basic stress diffusion solutions for fluid-saturated elastic porous-media with compressible constituents. *Reviews of Geophysics*, 14(2), 227–241. <https://doi.org/10.1029/RG014i002p00227>
- Rivard, C., Lavoie, D., Lefebvre, R., Séjourné, S., Lamontagne, C., & Duchesne, M. (2014). An overview of Canadian shale gas production and environmental concerns. *International Journal of Coal Geology*, 126, 64–76. <https://doi.org/10.1016/j.coal.2013.12.004>
- Roth, M. P., Harrington, R. M., & Liu, Y. (2018). Constraining geological structures and temporal variations in fluid accumulation near hydraulic fracturing injection sites in the western Canada sedimentary basin. Abstract S23A-0495 presented at 2018 Fall Meeting, AGU, Washington DC, 10-14 Dec, 2018.
- Scholz, C. H. (2002). *The mechanics of earthquakes and faulting* (2nd ed.). Cambridge, UK: Cambridge University Press.
- Schultz, R., Atkinson, G., Eaton, D. W., Gu, Y. J., & Kao, H. (2018). Hydraulic fracturing volume is associated with induced earthquake productivity in the Duvernay play. *Science*, 359(6373), 304–308. <https://doi.org/10.1126/science.aaa0159>
- Schultz, R., Corlett, H., Haug, K., Kocon, K., MacCormack, K., Stern, V., & Shipman, T. (2016). Linking fossil reefs with earthquakes: Geologic insight to where induced seismicity occurs in Alberta. *Geophysical Research Letters*, 43, 2534–2542. <https://doi.org/10.1002/2015GL067514>
- Segall, P., Grasso, J. R., & Mossop, A. (1994). Poroelastic stressing and induced seismicity near the Lacq gas field, southwestern France. *Journal of Geophysical Research*, 99(B8), 15,423–15,438. <https://doi.org/10.1029/94JB00989>
- Segall, P., & Lu, S. (2015). Injection-induced seismicity: Poroelastic and earthquake nucleation effects. *Journal of Geophysical Research: Solid Earth*, 120, 5082–5103. <https://doi.org/10.1002/2015JB012060>
- Sens-Schönfelder, C. (2008). Synchronizing seismic networks with ambient noise. *Geophysical Journal International*, 174(3), 966–970.
- Shapiro, S. A., & Dinske, C. (2009). Fluid-induced seismicity: Pressure diffusion and hydraulic fracturing. *Geophysical Prospecting*, 57(2), 301–310.
- Shelly, D. R., Beroza, G. C., & Ide, S. (2007). Non-volcanic tremor and low-frequency earthquake swarms. *Nature*, 446, 305–307.
- Shi, Y., & Bolt, B. A. (1982). The standard error of the magnitude-frequency value. *Bulletin of the Seismological Society of America*, 72, 1677–1687.
- Skempton, A. (1954). The pore-pressure coefficients A and B. *Geotechnique*, 4(4), 143–147.
- Skoumal, R., Brudzinski, M., & Currie, B. (2015). Earthquakes induced by hydraulic fracturing in Poland Township, Ohio. *Bulletin of the Seismological Society of America*, 105, 189–197. <https://doi.org/10.1785/0120140168>
- van der Elst, N. J., & Brodsky, E. E. (2010). Connecting near-field and far-field earthquake triggering to dynamic strain. *Journal of Geophysical Research*, 115, B07311. <https://doi.org/10.1029/2009JB006681>
- van der Elst, N. J., Savage, H. M., Keranen, K. M., & Abers, G. A. (2013). Enhanced remote earthquake triggering at fluid-injection sites in the midwestern United States. *Science*, 341(6142), 164–167. <https://doi.org/10.1126/science.1238948>
- Visser, R., Smith, B., Kao, H., Mahani, A. B., Hutchinson, J., & McKay, J. E. (2017). A comprehensive earthquake catalogue for northeastern British Columbia and western Alberta, 2014–2016, Geological survey of Canada, Open file 8335, 1.zip file. <https://doi.org/10.4095/306292>
- Waldhauser, F. (2001). hypoDD—A program to compute double-difference hypocenter locations (hypoDD version 1.0-03/2001; U.S. Geological Survey Open File Report, 01, 113). Reston, VA: USGS. <https://doi.org/10.3133/ofr01113>
- Waldhauser, F., & Ellsworth, W. L. (2000). A double-difference earthquake location algorithm: Method and application to the northern Hayward fault, California. *Bulletin of the Seismological Society of America*, 90(6), 1353–1368. <https://doi.org/10.1785/0120000006>
- Walter, J. I., Meng, X., Peng, Z., Schwartz, S. Y., Newman, A. V., & Protti, M. (2015). Far-field triggering of foreshocks near the nucleation zone of the 5 September 2012 (M<sub>w</sub> 7.6) Nicoya Peninsula, Costa Rica earthquake. *Earth and Planetary Science Letters*, 431, 75–86. <https://doi.org/10.1016/j.epsl.2015.09.017>
- Wang, B., Harrington, R. M., Liu, Y., Kao, H., & Yu, H. (2018). Remote dynamic triggering of earthquakes in three unconventional Canadian hydrocarbon regions based on a multiple-station matched-filter approach. *Bulletin of the Seismological Society of America*, 109(1), 372–386. <https://doi.org/10.1785/0120180164>
- Wang, B., Harrington, R. M., Liu, Y., Yu, H., Carey, A., & Elst, N. J. (2015). Isolated cases of remote dynamic triggering in Canada detected using cataloged earthquakes combined with a matched-filter approach. *Geophysical Research Letters*, 42, 5187–5196.
- Wang, R., & Kumpel, H.-J. (2003). Poroelasticity: Efficient modelling of strongly coupled, slow deformation processes in a multilayered half-space. *Geophysics*, 68(2), 705–717.

- Weingarten, M., Ge, S., Godt, J. W., Bekins, B. A., & Rubinstein, J. L. (2015). High-rate injection is associated with the increase in U.S. mid-continent seismicity. *Science*, *348*(6241), 1336–1340. <https://doi.org/10.1126/science.aab1345>
- Wiemer, S., & Wyss, M. (2000). Minimum magnitude of complete reporting in earthquake catalogs: Examples from Alaska, the western United States, and Japan. *Bulletin of the Seismological Society of America*, *90*(4), 859–869. <https://doi.org/10.1785/0119990114>
- Withers, M., Aster, R., Young, C., Beiriger, J., Harris, M., Moore, S., & Trujillo, J. (1998). A comparison of select trigger algorithms for automated global seismic phase and event detection. *Bulletin of the Seismological Society of America*, *88*(1), 95–106.
- Yao, H., Gouédard, P., Collins, J. A., McGuire, J. J., & van der Hilst, R. D. (2011). Structure of young East Pacific Rise lithosphere from ambient noise correlation analysis of fundamental-and higher-mode Scholte-Rayleigh waves. *Comptes Rendus Geoscience*, *343*(8-9), 571–583. <https://doi.org/10.1016/j.crte.2011.04.004>
- Yu, H., Liu, Y., Harrington, R. M., & Lamontagne, M. (2016). Seismicity along St. Lawrence paleorift faults overprinted by a meteorite impact structure in Charlevoix, Québec, Eastern Canada seismicity. *Bulletin of the Seismological Society of America*, *106*(6), 2663–2673.
- Zeng, X., Zhang, H., Zhang, X., Wang, H., Zhang, Y., & Liu, Q. (2014). Surface microseismic monitoring of hydraulic fracturing of a shale-gas reservoir using short-period and broadband seismic sensors. *Seismological Research Letters*, *85*(3), 668–677.
- Zoback, M. D., & Harjes, H. P. (1997). Injection-induced earthquakes and crustal stress at 9 km depth at the KTB deep drilling site, Germany. *Journal of Geophysical Research*, *102*(B8), 18,477–18,491. <https://doi.org/10.1029/96JB02814>